

DOI:

Evaluation of Probe-Material Thermal Interaction in Plasma Wind Tunnel Tests by Means of IR Thermography and Thermal Inverse Modelling

Andrea Fagnani*[†], Bernd Helber* and Olivier Chazot*

*von Karman Institute for Fluid Dynamics

Chaussée de Waterloo 72, 1640 Rhode-St-Genèse, Belgium

andrea.fagnani@vki.ac.be · helber@vki.ac.be · chazot@vki.ac.be

[†]Corresponding author

Abstract

The VKI Plasmatron facility allows to reproduce the high-enthalpy chemically reacting boundary layer over a re-entry body. Test conditions are suitable for qualification of thermal protection systems and material response studies. The present work combines numerical and experimental procedures to rebuild the thermal steady-state of the test probe subject to the plasma flow. The proposed analysis allows to account for multidimensional heat transfer effects in determining the stagnation point heat flux over the material sample. The technique is applied to metallic and silicon-carbide specimens, highlighting the main parameters which affect their thermal response.

1. Introduction

The atmospheric entry of a spacecraft at hypersonic speed is a fascinating engineering challenge, as it involves a broad range of scientific and industrial capabilities. One crucial aspect is the design and the implementation of the Thermal Protection System (TPS), which is needed to protect the spacecraft and its payload from the severe thermal and mechanical loads encountered during the planetary entry. In this context, the use of ground test facilities for TPS characterization and qualification becomes imperative. During the last decades, growing attention has been paid to arc-jet and induction type plasma wind tunnels, for their possibility to perform long duration, high-enthalpy tests.¹⁴ Arc jets are usually preferred for qualification testing of large-scale samples at very high heat flux, thanks to their high-power capabilities.¹¹ On the other hand, Inductively Coupled Plasma (ICP) facilities, using electrodeless technology for the plasma discharge generation, ensure a superior flow purity and are usually more dedicated to the study of aerothermochemistry and gas-surface interaction phenomena.³¹ TPS ground testing has a long experience at the von Karman Institute (VKI) for Fluid Dynamics, where interest has been devoted to the material response characterization in terms of catalytic behaviour, oxidation processes and ablation phenomena. The work of Panerai³¹ and Helber²² extensively treated reusable and ablative heat shield testing respectively.

Recently, in the course of the Design for Demise (D4D) strategy, promoted by the European Space Agency, the sound experience gained in TPS testing has been applied to study space debris materials. The D4D philosophy aims at reducing the risks associated with the ground impact of space debris through an appropriate design, by improving the break-up and demise mechanisms of any spacecraft component subjected to an uncontrolled atmospheric entry.³⁴ Plasma wind tunnel testing is herein crucial to develop and validate accurate models, suitable for predicting the thermal degradation process in re-entry conditions. However, space debris demise is a complex multi-physics phenomenon, typically encompassing all aspects of the gas-surface interaction processes. Moreover, the material classes of interest are broad, including silicates and metals, whose properties significantly differ from those of TPS materials, thus exhibiting widely varied responses towards re-entry environments.

In this framework, it is essential to improve the experimental set-up and the data-processing capabilities for the ground testing. Thus, in the present work, we introduce a numerical-experimental methodology to rebuild the thermal steady-state of the test probe subject to the plasma flow. The technique aims at improving the material response characterization, allowing to account for multidimensional heat transfer effects in the test material.

PROBE-MATERIAL THERMAL INTERACTION IN PLASMA WIND TUNNEL TESTS

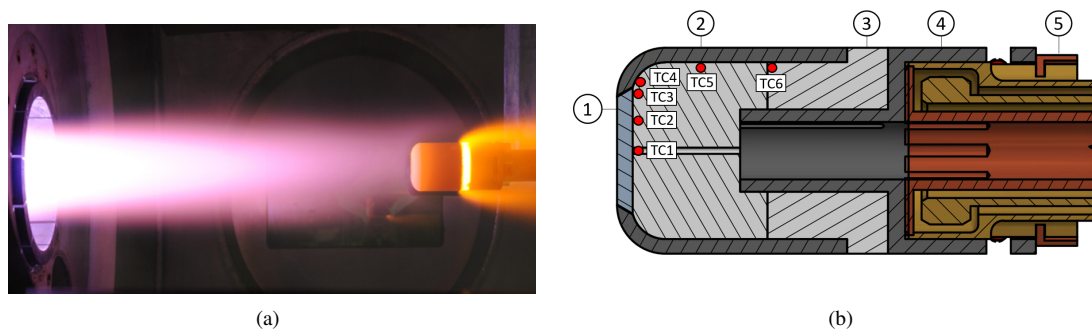


Figure 1: (a) Picture of the plasma jet impinging on the sample probe in the VKI Plasmatron facility. (b) Schematic of the sample probe, highlighting the sample material (1), the SiC-coated graphite cover (2) and the alumina-silica insulating element (3). A graphite mount (4) allows to secure the probe to a cooled support (5). Red circles represent the position of the ThermoCouple (TC) sensors, further explained in sec. 3.3.

1.1 Problem statement

The VKI Plasmatron is usually operated in subsonic regime, from which the complete reproduction of the actual flight conditions is achieved locally, at the stagnation point boundary layer, applying the local heat transfer simulation methodology,⁴ based on the Fay and Riddell¹⁷ and Goulard¹⁸ theory and extended to plasma wind tunnel testing by Kolesnikov.²⁵ Depending on the material properties to be studied, several geometries can be tested, ranging from hemispherical to coin-shaped samples. In this work we consider the latter geometry only. As depicted in fig 1(b), the sample material is inserted in a test probe and exposed to the plasma flow in stagnation point configuration. The probe is made up of a SiC-coated graphite cover, an insulating element (alumina-silica), a graphite mount and a cooled support. Receiving heat from the high-temperature plasma flow, heat exchange occurs within the probe body, driven by conduction towards the cooled holder and radiation from the probe surface. Until recently, the detailed thermal analysis of the probe was not performed and 1D or adiabatic wall assumptions were adopted to evaluate temperature gradients within the material sample and to determine surface heat fluxes. This simplifying hypotheses could provide practical results for reusable TPS materials.³¹ However, the higher thermal conductivity and the lower emissivity of metallic specimens,^{2,35} of interest for the D4D testing, can have a larger impact on the heat conduction inside the sample. The major drawback is that multidimensional heat transfer effects can arise, making the 1D heat transfer analysis no longer valid. Rather, a more sophisticated procedure, herein described, is required to correctly process the data and rebuild the quantities of interest.

1.2 Review of heat flux sensors

With the purpose of assessing the thermal interaction between the material sample and the probe body, one needs to determine the heat fluxes on the sample boundaries. Measuring heat fluxes requires a proper thermal sensor, its corresponding thermo-physical model and some temperature transducers.^{12,13} In standard techniques, where temperature is measured by thermocouples or resistance detectors, the transducer allows to determine the heat flux at a single point. One dimensional thermal models are usually employed to retrieve the heat flux, under the common hypothesis of constant thermophysical properties of the materials and negligible multi-dimensional effects. Yet, large temperature gradients and coupled phenomena, such as conduction-convection-radiation, make these methodologies unsatisfactory. The use of conventional techniques in high-enthalpy wind tunnels, in fact, where the latter phenomena are commonly encountered, has demonstrated several limitations.¹

On the other hand, InfraRed (IR) thermography represents a non-intrusive temperature transducer, able to provide a 2D projection of the temperature map on the observed object. Correspondingly, the heat flux sensor and its model may become multidimensional and temperature dependent thermal properties can be accounted for. Several studies can already be found in the literature, where heat flux sensors based on a numerical solution of Fourier's equation (typically described by an inverse heat transfer model) and surface temperature measurements were developed.¹² A physical mathematical model of a heat flux sensor, based on experimental data measured by means of IR thermography and on the numerical solution of the Fourier's equation in the test object, was proposed by Cardone⁹ and applied to plasma wind tunnel tests to estimate the stagnation point heat flux. Another example is provided by the work of Avallone et al.,¹ with application to convective heat transfer measurements in hypersonic flows. The Inverse Heat Transfer Problem (IHTP) in the test object was solved by means of a recursive least square technique, minimizing the

PROBE-MATERIAL THERMAL INTERACTION IN PLASMA WIND TUNNEL TESTS

difference between numerically computed temperatures and the experimental data provided by IR thermography.

More in detail, inverse heat transfer problems rely on temperature and/or heat flux measurements for the estimation of unknown quantities which appear in their mathematical formulation.³⁰ Different techniques are available for their solution.¹⁵ One common approach is to reformulate the IHTP as an identification problem, to be solved with optimization algorithms. Here, the solution of the Direct Heat Transfer Problem (DHTP) is considered to be dependent on some governing parameters, which are determined by imposing that the computed temperatures best agree with experimentally measured data and the best fit is typically achieved by an ordinary least squares criterion.

1.3 Objectives

In this work, we combine experimental and numerical analysis to rebuild the thermal steady-state of the probe under test conditions. A comprehensive experimental set-up, featuring both optical and intrusive measurement techniques, allows to determine surface and in-depth temperatures of the probe. A thermal model of the test probe is developed and computed numerically. An optimization procedure solves the IHTP until computed temperatures best agree with the experimental values. The heat balance over the material sample is then extracted, providing access to more detailed information on the thermal state of the material exposed to the plasma flow. The technique is then applied to determine the catalytic recombination coefficient of the test material samples, highlighting the improvements gained through the thermal analysis.

2. The VKI Plasmatron facility

The VKI Plasmatron is a high-enthalpy plasma facility, equipped with a 1.2 MW, 400 kHz, 2 kV MOS solid state generator. A schematic of the facility is shown in fig. 2. The plasma jet is generated in a 160 mm diameter quartz tube and expanded into a 1.4 m diameter, 2.5 m long test chamber, in which pressure is kept under atmospheric conditions through three rotating vanes vacuum pumps. The test gas is annularly injected in a quartz tube, which is surrounded by a coil in which high-voltage, high-frequency current is provided by the electrical generator. By electromagnetic field coupling, charged particles in the flow are induced to form eddy currents which, by Joule effect, result in the heating of the gas. The increased temperature forces the gas to expand and accelerate through the tube into the test chamber, where pressure is kept to a lower level with respect to the atmospheric conditions. As the gas is heated by electromagnetic induction, the advantage of ICP torches, with respect to arc-jet heaters, is primarily related the high purity of the plasma flow, due to the absence of electrodes and their associated erosion products. The uniquely large size plasma torch is suited for a broad range of test articles dimensions. Sample materials and jet-calibration probes are mounted onto cooled holders which can be remotely activated to be injected and retracted from the plasma jet. Suitable windows provide the necessary optical access, both lateral and front views, to the test chamber for the sample and flow diagnostics and they can be equipped with special crystals which allow high optical transparency in the spectral range of the measurement instruments.

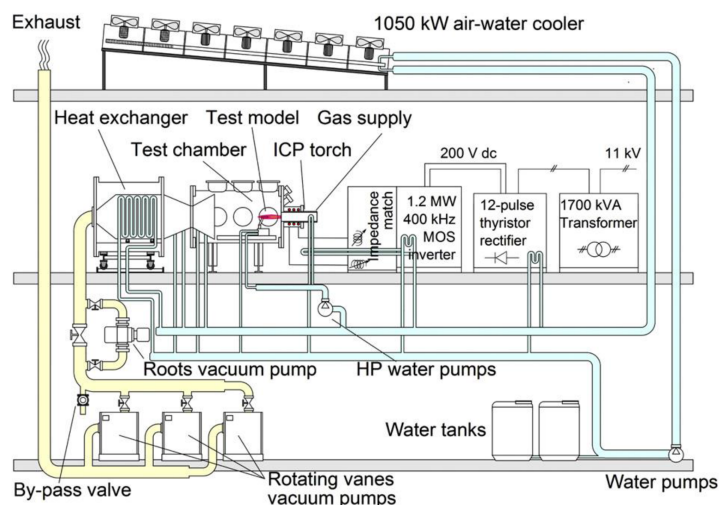


Figure 2: Schematic of the VKI Plasmatron facility.

PROBE-MATERIAL THERMAL INTERACTION IN PLASMA WIND TUNNEL TESTS

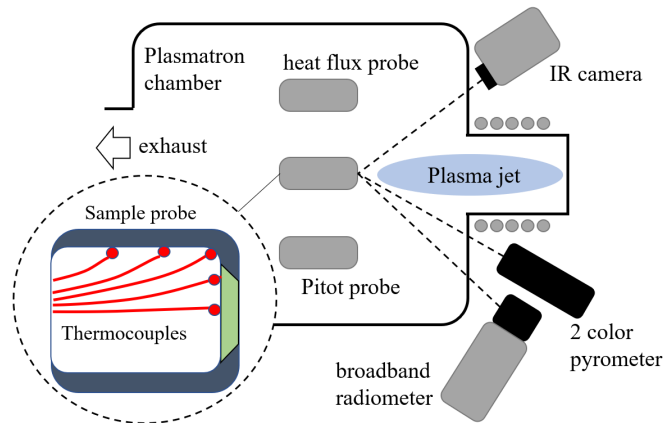


Figure 3: Schematic of the experimental set-up.

2.1 Plasma flow characterization

The characterization of the flow conditions in the VKI Plasmatron facility is performed by combining intrusive measurements techniques and suitable modelling. Static pressure in the Plasmatron chamber is measured by means of an absolute pressure transducer (Memberanovac DM 12, Leybold Vacuum). An auxiliary copper water-cooled probe, with the same geometry of the actual sample probe, provides the cold wall stagnation point heat flux (\dot{q}_{cw}) measured by a 14 mm diameter copper water calorimeter placed in the front face. A similar auxiliary probe, featuring a stagnation point pressure port, connected to a Validyne variable reluctance pressure transducer, allows to measure the flow dynamic pressure (p_{dyn}). The subsonic Plasmatron flow-field is then numerically simulated using an in-house magnetohydrodynamic solver (VKI ICP code^{28,32}), with the correspondent input electric power, static pressure and gas mass flow rate to the facility, allowing to characterize the boundary layer geometry around the test sample under local thermodynamic equilibrium and axisymmetric flow assumptions. Hydrodynamic parameters characterizing the flow boundary layer around the test probe are then extracted from this computation.²² These flow characteristics, as well as the experimentally determined heat flux and Pitot pressure serve as input conditions for the VKI boundary layer code.⁶ The latter solves the chemically reacting stagnation line boundary layer over a catalytic surface under chemical non-equilibrium conditions. A Newton method is used to iterate on the boundary layer outer edge temperature T_e , until experimental (\dot{q}_{cw}) and numerical heat fluxes are matched. The outputs of the whole procedure are the boundary layer outer edge plasma conditions (temperature T_e , enthalpy h_e and velocity gradient β_e) and free-stream velocity (u_{fs}).

3. Experimental set-up and measurement techniques

Fig. 3 depicts a schematic of the Plasmatron test chamber and the experimental set-up adopted in the context of this study. Heat flux and Pitot probes are used to calibrate the plasma flow conditions by measuring \dot{q}_{cw} and p_{dyn} . Two-colour pyrometry and radiometry are adopted for the surface temperature and emissivity characterization of the material sample, while IR thermography provides the temperature mapping of the sample probe surface. Additionally, the latter is internally instrumented with thermocouples in critical points for the thermal analysis.

3.1 Test sample materials

Two material samples are investigated in this study, namely, stainless steel AISI 316L (fig. 4 (a)) and carbon silicon carbide MTA C/SiC (fig. 4 (b)). The former is representative of metallic space debris, since metallic alloys are commonly employed for aerospace structures. The second material is the Keraman C/SiC produced by MT Aerospace in Augsburg, Germany. This is a Ceramic Matrix Composite (CMC) Carbon fiber reinforced Silicon Carbide (C/SiC) material, commonly used for reusable TPS. The dimensions of the samples are 26 mm external diameter, while the thickness is 3.8 mm and 3 mm respectively. To analyse the steady state heat balance, we target a surface temperature around 1400 K for both sample materials. This will avoid both melting of the metallic sample and active oxidation of the silicon-carbide material.

PROBE-MATERIAL THERMAL INTERACTION IN PLASMA WIND TUNNEL TESTS

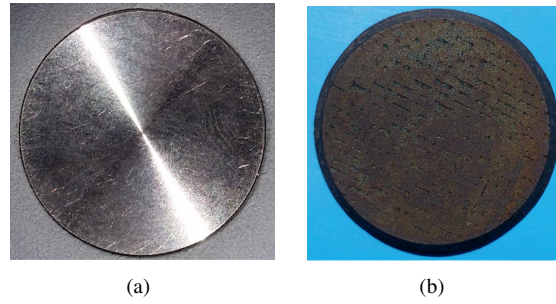


Figure 4: Pictures of the virgin sample materials tested for this study. Stainless steel AISI 316L (a) and carbon-silicon-carbide MTA C/SiC (b).

3.2 Sample probe surface radiometry

3.2.1 Surface temperature and total emissivity measurement on the material sample

A two-color pyrometer (Marathon Series MR1SB, Raytek Corp., Santa Cruz, CA, USA), with an operating range between 700°C and 1800°C, allows to measure the sample material surface temperature T_w . Optical access to the test chamber is offered through a 1 cm thick quartz window, placed at ~ 1 m distance to the probe, with an orientation of $\sim 35^\circ$ with respect to the sample surface normal. The measurement spot on the material specimen has an estimated elliptical shape with dimensions of ~ 5.6 mm major axis, ~ 4.6 mm minor axis.³¹ Acquisition frequency is set to 2 Hz. After calibration with a reference source, the measurement uncertainty on T_w is estimated to be $\pm 1.5\%$.

A broadband infrared radiometer (KT19, HEITRONICS Infrarot Messtechnik GmbH, Wiesbaden, Germany) is adopted to record the sample emitted radiation. It is positioned at a distance of ~ 1.1 m, with an inclination of $\sim 47^\circ$ with respect to the surface normal. Optical access to the Plasmatron chamber is offered through a 1.8 cm thick KRS-5 window (TlBr-TII), which offers $\sim 70\%$ optical transparency in the whole spectral range of the instrument (0.6 – 39 μm). The operating temperature range is between 0°C and 3000°C and the acquisition frequency is set to 1 Hz. The output signal is proportional to the integrated thermal radiation over such spectral range. Considering that, for the temperatures of interest in the Plasmatron facility ($T_w > 1000$ K), the bulk of the emitted radiation is contained in the spectral range between 0.6 and 39 μm , one can reasonably approximate the in-band radiance sensed by the radiometer with the total radiance, committing a negligible error³¹ ($\sim 0.1\%$). The radiometric signal is then converted into an equivalent temperature T_{radio} through

$$\int_{0.6 \mu\text{m}}^{39 \mu\text{m}} L(\lambda, T_w, \bar{\theta}, \bar{\phi}) d\lambda \approx \int_0^\infty L(\lambda, T_w, \bar{\theta}, \bar{\phi}) d\lambda = \frac{\sigma}{\pi} T_{\text{radio}}^4 \quad (1)$$

where $L(\lambda, T_w, \bar{\theta}, \bar{\phi})$ is the surface spectral radiance at wavelength λ , temperature T_w , along the direction identified by the angles $\bar{\theta}$ and $\bar{\phi}$, and σ is the Stefan-Boltzmann constant. From the definition of the total directional emissivity,³³ one can determine

$$\varepsilon^{\text{tot}}(T_w, \bar{\theta}, \bar{\phi}) = \frac{T_{\text{radio}}^4}{T_w^4}. \quad (2)$$

In principle, due to the inclination of the radiometer with respect to the sample surface normal, one obtains only a directional value, valid for $\bar{\theta}$ and $\bar{\phi}$. If we consider the surface to exhibit a lambertian behaviour and that emissivity generally decreases for very sharp angles for the materials here treated (oxidised steel⁷ and SiC³¹) we can assume our measurement to be representative of the total hemispherical emissivity ε^{tot} with good approximation. After calibration with a reference source, the measurement uncertainty on T_{radio} is estimated to be $\pm 1\%$. In conclusion, accounting for the uncertainties on T_w and T_{radio} , one can estimate the uncertainty on the measured emissivity value to be $\pm 7\%$.

3.2.2 Infrared thermography and temperature map reconstruction on 3D surfaces

The ThermaCAM SC3000 (FLIR SYSTEM, Hong Kong) infrared thermocamera is used to assess the temperature distribution over the sample and probe surfaces. It is equipped with a GaAs Quantum Well Infrared Photodetector (QWIP) sensor with a resolution of 320x240 pixels and a maximum spectral sensitivity in the long-wavelength infrared range between 7 μm and 9 μm . The temperature range for the camera is 350-1500°C and the acquisition rate is set to 2 Hz. The camera is placed at ~ 1 m distance from the probe, with an inclination of $\sim 47^\circ$ with respect to the sample

PROBE-MATERIAL THERMAL INTERACTION IN PLASMA WIND TUNNEL TESTS

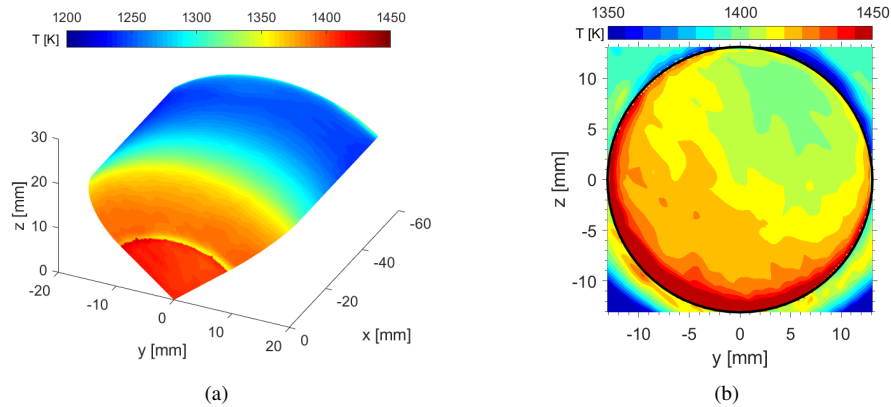


Figure 5: Example of temperature map reconstruction on the sample probe: 3D slice over the sample and cover (a); 2D projection over the whole material specimen (b). The black circle in image (b) represents the sample boundary.

surface normal and optical access to the Plasmatron chamber is assured through a 1.8 cm thick KRS-5 window. Specific procedures allow the in situ measurement of the in-band emissivity $\varepsilon_{\Delta\lambda}$ and its temperature dependent correction.¹⁶

After proper intensity calibration and emissivity correction, IR thermography provides a two-dimensional projection of the object temperature map. To exploit the multidimensional temperature information for quantitative measurements, however, it is required to establish the correspondence between the points of the observed object and the pixels of the thermal image.¹⁰ To this purpose, a dedicated geometrical calibration technique has been introduced for the Plasmatron IR data analysis in the context of this work. The geometrical calibration model exploits the camera calibration toolbox developed by Bouguet,⁸ which is based on the perspective projection model with lens distortion proposed by Heikkilä.²¹ Its purpose is to determine a set of camera parameters that describe the mapping between 3D reference coordinates and 2D image pixels. To establish this correspondence, a suitable calibration target is placed on the probe body before the test. Once the geometrical calibration of the camera is performed, one is able to rebuild a 3D temperature map on the test object, as shown in Figure 5. In particular, the viewing angle allows to see the whole material sample (Fig. 5 (b)), while only a 90° slice of the probe cover can be reconstructed (Fig. 5 (a)).

3.2.3 Plasma radiation interference

The high temperature plasma is a strong emitter of electromagnetic radiation, which may pollute the radiometric measurements; thus, it is required to identify possible sources of undesired interferences. Current efforts are being undertaken at VKI to quantify in detail the effect of the plasma emission on the radiometric measurements. In particular, the temperature distribution along the line-of-sight of the instrument is extracted from the numerical simulation of the plasma flow field, accomplished with the VKI ICP CODE (see sec. 2.1). The radiative transfer equation is then solved along the slab and the plasma emission is compared to the surface radiance. Preliminary results show that the plasma transmissivity in the wavelength ranges of interest is close to one. Moreover, for the steady-state temperature measurement, the influence of the plasma emission can be considered negligible over a broad range of test conditions.

3.3 Thermocouple thermometry

At the interface between the sample and the cover (see fig. 5 (a)), the IR measurement loses effectiveness. Due to the transition between different materials, emissivity and surface temperature can change sharply. However, owing to the finite spatial resolution of the IR camera, this effect is smeared out significantly in the actual measurement. Since this interface is critical to retrieve the correct heat balance over the sample, type K thermocouples are additionally placed on the internal surface of the sample and probe cover in order to recover reliable information. Their main purpose, then, is to provide a better resolution of the temperature jump between the two parts. Three thermocouples are placed on the sample back surface and three additional sensors are placed on the cover back surface. A sketch of the position of the thermocouples was shown in fig. 1 (b).

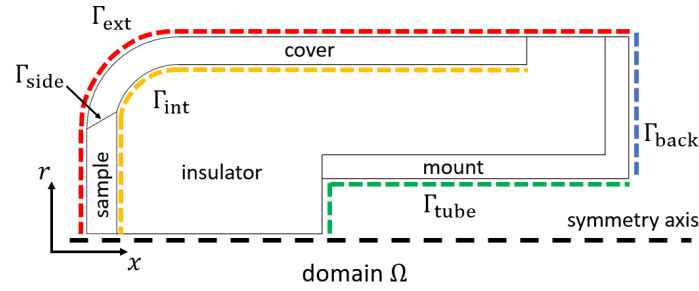


Figure 6: Sketch of the numerical domain, highlighting the most significant boundaries for the thermal analysis.

4. Thermal modelling of the sample probe

A thermal model of the steady-state heat transfer in the sample probe was developed and numerically solved in FREEFEM++,²⁰ a high-level, open-source environment for finite element discretization of partial differential equations. The numerical domain Ω (sketched in fig. 6) is made up of four different regions, including the material sample, the cover, the insulating element and the mount. Several boundaries are highlighted: external (Γ_{ext}), back (Γ_{back}), inner tube (Γ_{tube}) and sample side (Γ_{side}). In addition, the boundary Γ_{int} , encompassing the sample and the cover internal surfaces, will become useful when discussing the results.

4.1 Formulation of the thermal problem

Letting T be the temperature field, k be the thermal conductivity, \mathbf{n} the outgoing normal to the boundary Γ of the domain Ω (fig. 6), the weak form of the axisymmetric steady thermal problem in cylindrical coordinates, with the test function v , is the following^{26,27}

$$\int_{\Omega} 2\pi r (k \nabla T \cdot \nabla v) - \int_{\Gamma} 2\pi r (k \nabla T \cdot \mathbf{n}) \cdot v = 0 \quad \text{in } \Omega. \quad (3)$$

As far as the boundary conditions on the probe external surface are concerned, one can either choose to impose a surface temperature distribution, i.e., $T = T_{\text{ext}}$ on Γ_{ext} , or impose a heat flux distribution and allowing cooling by radiation. In this case, the surface energy balance allows to write

$$\dot{q}_w^{\downarrow} = \dot{q}_{\text{conv}}^{\downarrow} + \dot{q}_{\text{diff}}^{\downarrow} = \dot{q}_{\text{cond}} + \dot{q}_{\text{rad}}. \quad (4)$$

That is, the heat flux released from the gas to the surface \dot{q}_w^{\downarrow} , which is made up of a convective part $\dot{q}_{\text{conv}}^{\downarrow}$ and a diffusive part⁵ $\dot{q}_{\text{diff}}^{\downarrow}$ (due to heterogeneous chemical reactions), is balanced by the conduction inside the material \dot{q}_{cond} and radiation away from the surface \dot{q}_{rad} . Making the right hand side of the last equation explicit, one obtains the boundary condition

$$k \frac{\partial T}{\partial n} + \sigma \varepsilon (T^4 - T_{\text{amb}}^4) - \dot{q}_w^{\downarrow} = 0 \quad \text{on } \Gamma_{\text{ext}}, \quad (5)$$

where σ is the Stefan-Boltzmann constant, ε the total hemispherical emissivity and $T_{\text{amb}} = 350$ K is the ambient temperature towards which the probe radiates. The cooling by the probe holder on the back surface is modelled as a convection to an isothermal surface of temperature $T_{\text{cool}} = 350$ K. The boundary Γ_{tube} , instead, is assumed to be adiabatic. Owing to the axisymmetric formulation, no boundary condition is required on the axis, as the bilinear forms in eq. 3 degenerate at $r = 0$. A finite element discretization is adopted for the numerical solution of the problem. The mesh includes ~ 30000 elements and a convergence study demonstrated that this number is sufficient for the solution not to be affected. As the variation of the material thermal properties in the temperature range of interest for Plasmatron applications can be extremely significant, the model is able to account for orthotropic (i.e., different values in the r and x directions) and temperature dependent thermal properties. Reference values of thermal conductivities for steel AISI 316L,²⁴ Keraman C/SiC,³ graphite¹⁹ and alumina-silica¹⁶ are used for the thermal analysis.

4.2 Thermal contact conductance issues

Contact resistance between different parts of the probe can play a significant role in the thermal analysis. The Thermal Contact Conductance (TCC) coefficient \hat{h}_{TCC} , that is, the inverse of the thermal contact resistance, is defined as the

PROBE-MATERIAL THERMAL INTERACTION IN PLASMA WIND TUNNEL TESTS

ratio between the heat flux between the two surfaces, \dot{q} , and the temperature difference ΔT established at the interfaces due to the imperfect joint:²⁷

$$\hat{h}_{\text{TCC}} = \frac{\dot{q}}{\Delta T}. \quad (6)$$

Since this parameter depends on several factors, such as the specific materials involved, surface roughness and oxidation status, contact pressure, temperature and interstitial fluid pressure,²⁷ it is extremely difficult to model correctly. Hence, in the probe manufacturing, the material sample and the cover are glued to the insulator; as a result, one can reasonably assume perfect thermal contact along the interface on Γ_{int} . Yet, the sample-cover interface on Γ_{side} is not glued since the effect of the TCC can be beneficial in providing insulation of the material specimen from the highly conductive cover and limiting the heat exchange. Hence, in the numerical model, a temperature discontinuity is allowed on this interface, driven by the heat transfer coefficient \hat{h}_{TCC} .

5. Methodology for the solution of the inverse heat transfer problem

From the mathematical formulation of the thermal problem, we can identify the objective parameters of the IHTP as:

- the heat flux $\dot{q}_w^\downarrow(x, r)$ on the external probe surface Γ_{ext} ;
- the TCC coefficient, \hat{h}_{TCC} , at the sample-cover interface, on Γ_{side} .

As far as $\dot{q}_w^\downarrow(x, r)$ is concerned, this is typically represented in the literature as a series of polynomials or sinusoidal functions and the IHTP is solved for the discrete coefficient of the expansion.¹ In the present work, instead, we choose to experimentally determine the profile shape of $\dot{q}_w^\downarrow(x, r)$, thus reducing its functional dependence to two parameters only, as explained hereafter.

5.1 Determination of the heat flux profile shape

In order to determine the profile shape of $\dot{q}_w^\downarrow(x, r)$ on the probe surface Γ_{ext} , an auxiliary experiment is performed. A similar probe with the same external geometry is subjected to similar flow conditions in which the sample material test has to be performed. This auxiliary probe features a plane cover, i.e., without sample material, as sketched in fig. 7. The surface temperature is then measured by IR thermography and applied as a boundary condition in the thermal model on the probe external surface (i.e., $T = T_{\text{IR}}$ on Γ_{ext}), after adequate spatial filtering. The numerical domain is adjusted accordingly to represent this probe geometry. The heat equation is then solved in the test probe to provide the conductive heat flux \dot{q}_{cond} on the boundary Γ_{ext} . Then, using equation 4, one obtains

$$\dot{q}_{\text{cond}} + \underbrace{\sigma \varepsilon T_{\text{IR}}^4}_{\dot{q}_{\text{rad}}} = \dot{q}_w^\downarrow \text{ on } \Gamma_{\text{ext}}. \quad (7)$$

Once the conduction term is computed and the radiation heat flux is determined from the measured emissivity coefficient ε and surface temperature T_{IR} , one can determine the spatially resolved heat flux $\dot{q}_w^\downarrow(x, r)$ on the probe boundary. The measured profile shapes of $\dot{q}_w^\downarrow(x, r)$, normalized to its stagnation point value, for the two test conditions (T1 and T2) to be performed in this work are represented in fig. 8 (a).

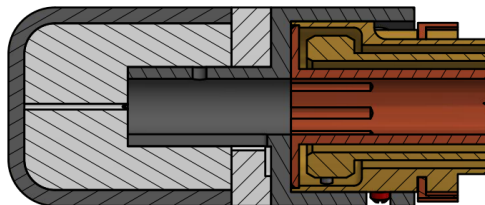


Figure 7: Sketch of the probe used to determine the heat flux profile shape. Notice the plane cover, without sample material.

A two parameter functional dependence is then introduced to use this profile shape in the IHTP. The first parameter is the stagnation point heat flux on the sample material, which we call $\dot{q}_{0\text{sample}}^\downarrow$. Moreover, in the actual experiment, the sample and the probe cover are made up of different materials. Then, the well documented phenomenon of the catalytic transition³¹ should be also considered. That is, due to the different heterogeneous reaction rates, $\dot{q}_{\text{diff}}^\downarrow$ can

PROBE-MATERIAL THERMAL INTERACTION IN PLASMA WIND TUNNEL TESTS

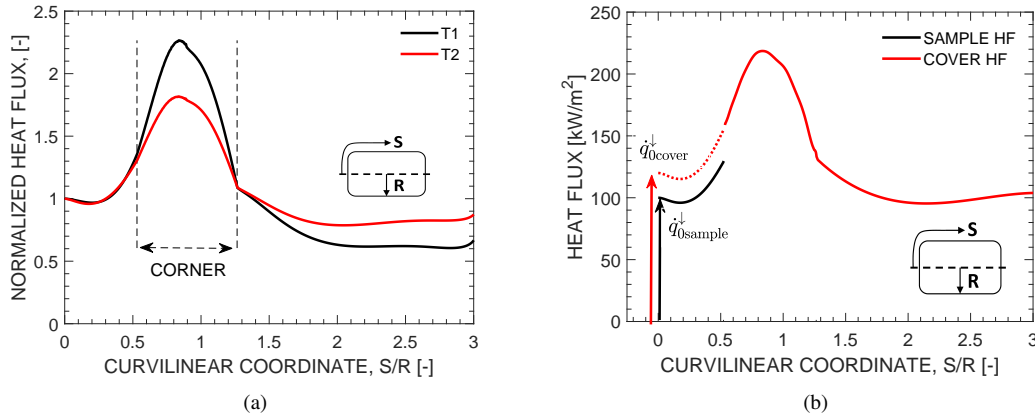


Figure 8: (a) Normalized heat flux profiles with respect to the stagnation point ($S = 0$) value, determined for the two test conditions (T1 and T2) to be performed in this work. (b) Example of heat flux profile used for the IHTP, highlighting the meaning of $\dot{q}_{0sample}^\downarrow$ and $\dot{q}_{0cover}^\downarrow$.

undergo a significant variation at the interface between the two materials. To account for this important effect, another variable is introduced, namely $\dot{q}_{0cover}^\downarrow$. As a result, the profile shape of \dot{q}_w^\downarrow is locally preserved on the sample and on the probe cover, but a discontinuity between them is allowed, as represented in fig. 8 (b). In conclusion, one can write the two-parameter functional dependence as $\dot{q}_w^\downarrow = \dot{q}_w^\downarrow(\dot{q}_{0sample}^\downarrow, \dot{q}_{0cover}^\downarrow)$.

5.2 Formulation of the identification problem

From the previous analysis, one concludes that the solution of the heat equation in the probe depends on three main parameters: $\dot{q}_{0sample}^\downarrow$ and $\dot{q}_{0cover}^\downarrow$ determine the actual magnitude of the heat flux on the probe external surface, while \hat{h}_{TCC} represents the contact conductance at the sample-cover interface. These variables are determined by minimizing the function

$$\mathfrak{F}(\dot{q}_{0sample}^\downarrow, \dot{q}_{0cover}^\downarrow, \hat{h}_{TCC}) = \sum [T_{ext} - T_{IR}]^2 + \sum [T_{int} - T_{TC}]^2, \quad (8)$$

where T_{IR} and T_{TC} are the experimentally measured temperatures by means of IR thermography and thermocouples, while T_{ext} and T_{int} are the numerically computed values in the corresponding locations, on the external (Γ_{ext}) and internal (Γ_{int}) probe boundaries respectively. The objective function is minimized by means of an hybrid optimization procedure. For a detailed description of this method, the reader is addressed to the work of Orlande et al.¹⁵ Here it suffices to say that a genetic algorithm is first used to produce an approximated solution, searching in a wide variable domain; hence, a gradient based algorithm provides a more accurate refinement towards the minimum of \mathfrak{F} . Letting $\mathbf{u} = [\dot{q}_{0sample}^\downarrow, \dot{q}_{0cover}^\downarrow, \hat{h}_{TCC}]$ be the set of variables, convergence is reached if, between two subsequent iterations, both the step size $\delta\mathbf{u}$ and the objective function variation $\mathfrak{F}(\mathbf{u} + \delta\mathbf{u}) - \mathfrak{F}(\mathbf{u})$ are lower than 10^{-6} .

6. Results

Two separate tests were performed in air plasma on the candidate materials, each one allowing ~ 600 s exposure of the samples to the plasma flow. The Plasmatron operating conditions are reported in table 1. The computed boundary layer edge conditions, provided by the method outlined in section 2.1, are additionally given in this table. The uncertainty on the numerically rebuilt quantities is based on propagation methods starting from the experimental data, following the procedure documented in reference.³¹

Measured surface temperature histories and emissivity values of the material samples are shown in Fig. 9. Reading of the surface temperature from the two-color pyrometer starts around $T_w \approx 1150$ K. For test T1 on the stainless steel sample (Fig. 9 (a)), T_w peaks around 1400 K during the transient heating; afterwards it decreases, reaching an average steady-state value of 1352 K. This phenomenon is believed to be caused mainly by oxidation, which, correspondingly, significantly changes the emissivity of the surface. This behaviour is correctly captured in the measured total and in-band emissivity coefficients, which increase considerably from ~ 0.2 up to ~ 0.9 at steady-state. Test T2 on the MTA C/SiC sample (Fig. 9 (b)), instead, was performed targeting two different surface temperatures,

PROBE-MATERIAL THERMAL INTERACTION IN PLASMA WIND TUNNEL TESTS

Table 1: Plasmatron operating conditions in air plasma, including numerical rebuilding. Static pressure p_s , cold-wall heat flux \dot{q}_{cw} , dynamic pressure p_{dyn} and generator power \mathbb{P}_{el} . The numerical boundary layer simulation provided edge enthalpy h_e and temperature T_e , as well as the free-stream velocity u_{fs} .

ID	Sample	Experimental data				Numerical rebuilding		
		p_s mbar	\dot{q}_{cw} kW/m ²	p_{dyn} Pa	\mathbb{P}_{el} kW	h_e MJ/kg	T_e K	u_{fs} m/s
T1	AISI 316L	102 ± 10	211 ± 48	11.9 ± 2.2	128	6.72 ± 1.49	3394 ± 381	49.7 ± 5.2
T2	MTA C/SiC	15.5 ± 1.5	414 ± 61	116.9 ± 11.7	145	10.30 ± 1.49	4471 ± 345	474.2 ± 40.7

Table 2: Summary of the hot wall conditions on the material samples. Values refer to average steady-state quantities, considering the last 100 s of the tests. ThermoCouples (TC) nomenclature with reference to fig. 1 (b).

ID	Sample	T_w K	T_{TC1} K	T_{TC2} K	T_{TC3} K	$\hat{\varepsilon}^{tot}$ -	$\varepsilon_{\Delta\lambda}$ -	\dot{q}_{rad}^{exp} kW/m ²
T1	AISI 316L	1352 ± 20	1318 ± 13*	1308 ± 13*	1288 ± 13*	0.90 ± 0.06	0.88 ± 0.02	169 ± 16
T2	MTA C/SiC	1410 ± 21	1371 ± 14*	1385 ± 14*	1353 ± 14*	0.91 ± 0.07	0.84 ± 0.02	203 ± 19

* Without considering systematic errors

namely, $T_w \approx 1300$ K for the first ~ 300 s and $T_w \approx 1400$ K for the last ~ 300 s. This procedure was prescribed by a dedicated test campaign on the material. For the purpose of this study, however, we only consider the second steady-state condition achieved. We can notice that, contrary to the AISI 316L sample, the temperature history on the MTA C/SiC is monotonically increasing and emissivity coefficients vary only slightly in the spanned temperature range. Overall, the measured emissivity values on both the metallic and carbon-ceramic materials compare very well with literature data from Balat et al.⁷ and Panerai.³¹ A summary of the hot wall conditions on the sample materials are further reported in table 2, also listing the values of the thermocouple temperatures on the samples back surface (T_{TC1} , T_{TC2} and T_{TC3}). $\varepsilon_{\Delta\lambda}$ refers to the in-band emissivity in the spectral range of the IR camera. The radiative heat flux is computed starting from the total hemispherical emissivity and wall temperature as $\dot{q}_{rad}^{exp} = \sigma \hat{\varepsilon}^{tot} T_w^4$. All the experimental data refer to average steady-state values, which include the last 100 seconds of exposure to the plasma flow.

We can notice that $T_w - T_{TC1}$ is about 30 K for test T1 and about 40 K for test T2. This temperature difference, however, is not physically consistent. If we take test T1, for example, we can estimate the conductive heat flux in the sample as

$$\dot{q}_{cond} \approx k \frac{T_w - T_{TC1}}{\Delta x} = 268 \text{ kW/m}^2, \quad (9)$$

where $k \approx 30$ W/m/K is the thermal conductivity of the material and $\Delta x = 3.8$ mm is the sample thickness. Then, recalling eq. 4, the heat balance on the sample surface reads

$$\dot{q}_w^\downarrow = \dot{q}_{cond} + \dot{q}_{rad}^{exp} = 437 \text{ kW/m}^2, \quad (10)$$

which is more than double with respect to the cold-wall heat flux \dot{q}_{cw} . Since \dot{q}_{cw} is measured on a high-catalytic cold-wall surface, this generally represents an upper bound for the achievable heat fluxes in plasma wind tunnels.^{22,31} Hence we conclude that a bias between thermocouple and radiometric measurements is present. Surface temperature measurements with thermocouples can be extremely troublesome. For instance, thermal contact resistance between the sensor junction and the surface can cause a temperature gradient which will prevent the thermocouple from attaining the correct value.²³ Moreover, systematic errors caused by the mounting scheme can easily become the largest source of uncertainty in extreme thermal environments²⁹ ($T > 1000$ K). Since thermocouples still bring valuable information about the temperature discontinuity between sample and probe cover, for the purpose of this study we will only consider their normalized value with respect to TC1, i.e., $\tilde{T}_{TCi} = T_{TCi}/T_{TC1}$. The radiometric temperature measurements, instead, will be preserved in their absolute value.

Simultaneously, the IR camera is used to record the surface temperature over the entire sample probe. Geometrical calibration is then applied to the thermograms, as explained in section 3.2.2, allowing to rebuild the 3D radiation map over the sample probe. Calibration and correction for the measured in-band emissivity $\varepsilon_{\Delta\lambda}$ of the sample material and probe cover are then applied. As far as the latter quantity is concerned, $\varepsilon_{\Delta\lambda}^{cover}$ was obtained separately in dedicated tests.¹⁶ The rebuilt temperature map over the probe surface is then spatially averaged (in the angular direction), in order to extract the most significant temperature profile to be compared with the axisymmetric thermal model. In particular, a 60° slice is averaged over the probe cover, while the whole 360° view is averaged over the material sample.

PROBE-MATERIAL THERMAL INTERACTION IN PLASMA WIND TUNNEL TESTS

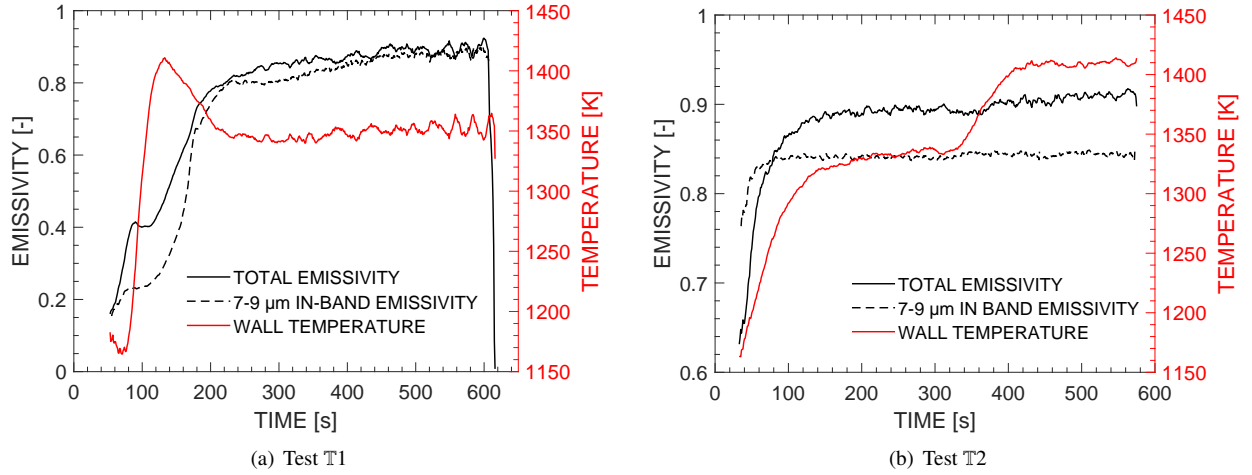


Figure 9: Evolution of the material total and in-band emissivities and surface temperature versus time from injection for test T1 (a) and T2 (b).

Table 3: Results of the inverse heat transfer problem.

ID	$\dot{q}_{0\text{sample}}$ kW/m ²	$\dot{q}_{0\text{cover}}$ kW/m ²	\hat{h}_{TCC} W/m ² .K
T1	199	88	208
T2	206	141	98

The methodology explained in sec. 5 is then applied for solution of the IHTP. The averaged IR temperature profile, along with the thermocouple data (normalized with respect to TC1), represent the input for the optimization problem. The heat flux profile shapes of $\dot{q}_w^\downarrow(x, r)$, instead, were obtained in dedicated auxiliary tests, as explained in sec. 5.1, reproducing similar plasma flow conditions as reported in table 1.

Figures 10 and 11 show the measured IR and thermocouple data, as well as the correspondent solution of the IHTP for test T1 and T2 respectively. One can observe that both the IR data and the normalized thermocouples values show higher temperatures for the sample with respect to the cover. In particular, from TC3 and TC4, which were placed at the sample-cover interface, a discontinuity in temperature is observed between the two materials; a phenomenon which is typical of contact resistance effects. As far as test T1 is concerned, both the averaged IR profile, as well as the discrete thermocouple measurements, show a temperature decrease from the axis towards the sample edge, suggesting heat losses towards Γ_{side} . On the other hand, this effect is less pronounced for test T2. Overall, the computed temperatures agree well in absolute value with the measured IR data on the boundary Γ_{ext} and in relative value with the measured thermocouple data on Γ_{int} . For test T1, a deviation with respect to the IR data is noticed towards $S/R > 2.5$. However, since this is far from Γ_{side} , no significant effect is expected on the estimation of the thermal balance over the sample material. For test T2, instead, the model temperature on Γ_{int} deviates with respect to T_{TCC5} ; yet, a good agreement is still achieved with the IR data on Γ_{ext} .

The parameters resulting from the solution of the IHTP are listed in tab. 3. In particular, $\dot{q}_{0\text{sample}}$ represents the estimated value of the stagnation point heat flux \dot{q}_w^\downarrow received by the material sample. Recalling the heat balance over the sample surface, one can write $\dot{q}_w^\downarrow = \dot{q}_{\text{cond}} + \dot{q}_{\text{rad}}$, then it is interesting to compare this quantity with the experimental value of $\dot{q}_{\text{rad}}^{\text{exp}} = \sigma \hat{\epsilon}^{\text{tot}} T_w^4$ from table 2. For test T1 on the metallic sample, $\dot{q}_{0\text{sample}}$ is $\sim 18\%$ larger than the measured radiative heat flux only, indicating that significant heat conduction effects are present. For test T2 on the silicon-carbide sample, instead, $\dot{q}_{0\text{sample}} \approx \dot{q}_{\text{rad}}^{\text{exp}}$, thus meaning that heat conduction in the sample is negligible. Furthermore, the fact that $\dot{q}_{0\text{sample}} > \dot{q}_{0\text{cover}}$ suggests a catalytic transition between the material sample and the cover. As expected from the literature,³¹ this transition is more important for the metallic sample, rather than for the silicon-carbide material.

The rebuilt thermal balance on the material samples for tests T1 and T2 are reported in fig. 12. For the metallic specimen (test T1), $\sim 30\%$ of the power released to the sample surface is conducted inside the material and only $\sim 70\%$ is radiated away from the surface. We must notice that the average heat conduction on the sample is larger than the one registered in the stagnation point only, owing to the radial increase in heat flux (see fig. 8). Only ~ 4 W are lost towards the sample back surface while the larger quota, i.e., ~ 33 W, is lost on the side surface. Here, even if a temperature jump

PROBE-MATERIAL THERMAL INTERACTION IN PLASMA WIND TUNNEL TESTS

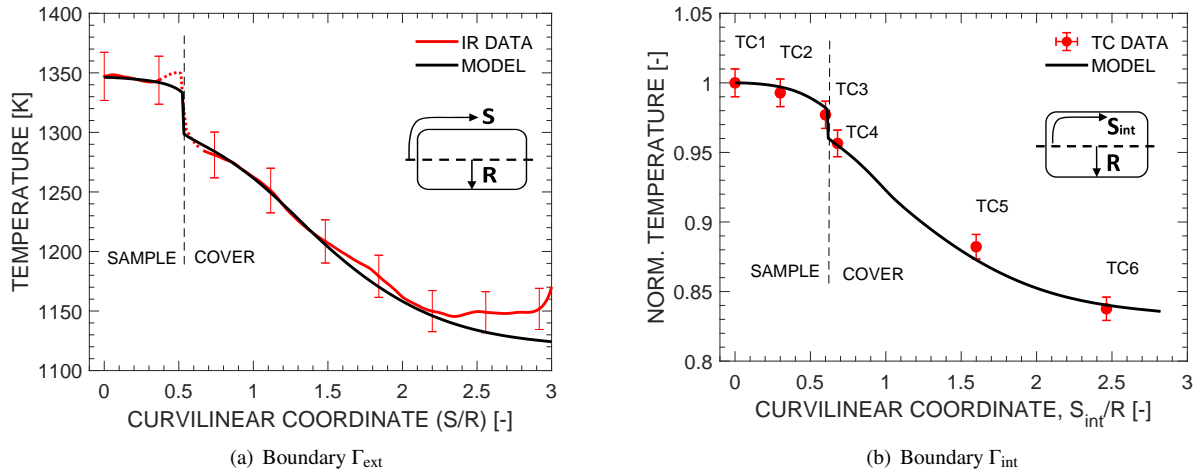


Figure 10: Solution of the IHTP for test T1 (AISI 316L sample), comparing the temperatures computed by the thermal model with IR data on Γ_{ext} (a) and with thermocouple values on Γ_{int} (b). Thermocouple data are normalized with respect to T_{TC1} and the numerical solution is normalized to the point $S_{int} = 0$.

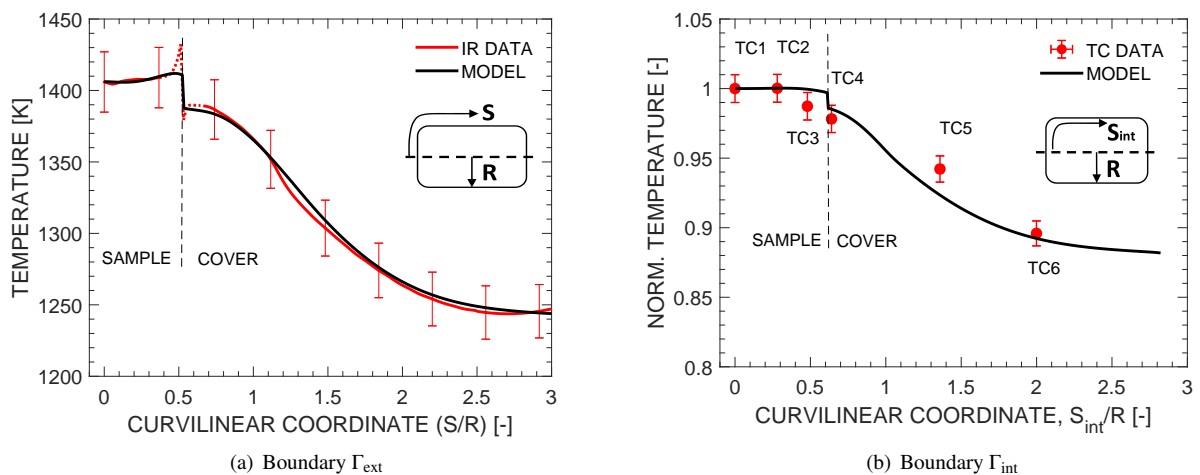


Figure 11: Solution of the IHTP for test T2 (MTA C/SiC sample), comparing the temperatures computed by the thermal model with IR data on Γ_{ext} (a) and with thermocouple values on Γ_{int} (b). Thermocouple data are normalized with respect to T_{TC1} and the numerical solution is normalized to the point $S_{int} = 0$.

PROBE-MATERIAL THERMAL INTERACTION IN PLASMA WIND TUNNEL TESTS

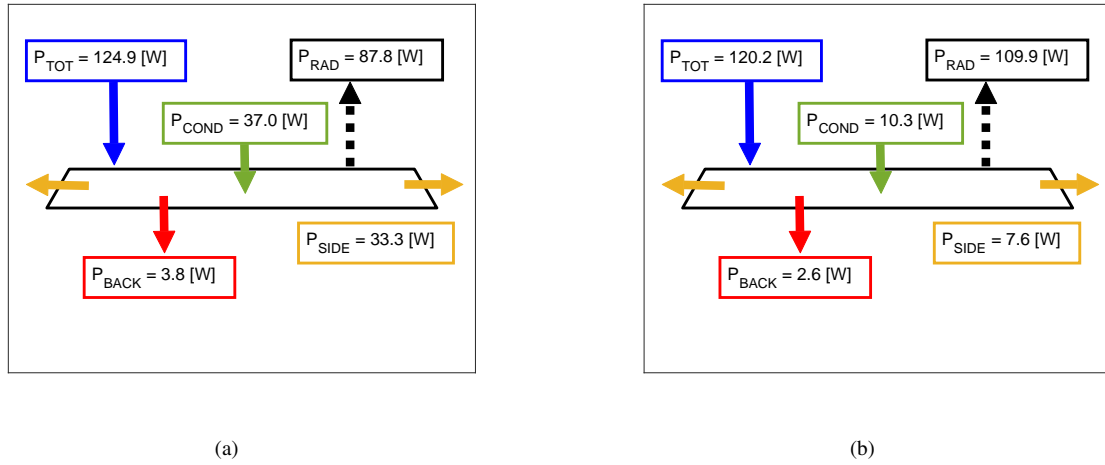


Figure 12: Heat rate balance on the sample materials as a result of the IHTP for test T1 (a) and T2 (b).

was observed, the radial temperature decrease on the sample drives significant heat to cover, which easily captures it due to the high thermal conductivity of graphite. As a result, one can conclude that the probe configuration does not ensure 1D heat transfer in this condition and multidimensional effects have to be accounted for.

For test T2, instead, the radial temperature gradient on the sample is less significant. As a result, as one can see from fig. 12 (b), the thermal interaction with the cover is smaller than the one registered for stainless steel. Average conduction in the sample represents only $\sim 8\%$ of the total received power and the adiabatic wall assumption could be a reasonable approximation in this case.

6.1 Application to the catalytic coefficient determination

Measuring the catalytic properties of materials subjected to atmospheric entry, thus quantifying the exothermic recombination of oxygen and nitrogen atoms into molecules on the surface, is essential for the accurate prediction of the heat flux released by the plasma flow to the material. Specific procedures allow to determine the catalytic recombination coefficient of a material sample in the VKI Plasmatron. For more details about the methodology, the reader is addressed to the work of Panerai.³¹ Here it suffices to say that, starting from the measured boundary layer edge conditions of the plasma flow around the test body, explained in sec. 2.1, the VKI boundary layer code can be employed in a second step to determine the sample material catalytic coefficient γ by matching the stagnation point heat flux, measured in experimental conditions, with the one numerically computed. Previous work^{22,31} assumed negligible conduction inside the material sample, thus, recalling eq. 4, one could approximate $\dot{q}_w^\downarrow \approx \dot{q}_{rad}^{exp}$. However, following the procedure described in this study, we are now able to provide a better estimate as $\dot{q}_w^\downarrow = \dot{q}_{0sample} = \dot{q}_{cond} + \dot{q}_{rad}$, also including the heat conduction in the sample material. Table 4 reports the results of the catalytic coefficient determination for the two material samples, comparing the results obtained by assuming adiabatic wall (i.e., $\dot{q}_w^\downarrow \approx \dot{q}_{rad}^{exp}$) and using the thermal analysis here presented (i.e., $\dot{q}_w^\downarrow = \dot{q}_{cond} + \dot{q}_{rad}$). We can conclude that for the silicon-carbide sample, a negligible correction on the catalytic coefficient γ is introduced by the thermal analysis. However, the conductive heat flux for the metallic specimen is significant and the catalytic coefficient increases by almost four times when the conduction effect is accounted for.

Table 4: Thermal analysis correction on the catalytic coefficient determination.

ID	Sample	Adiabatic wall assumption		Thermal analysis	
		$\dot{q}_w^\downarrow \approx \dot{q}_{rad}^{exp}$ kW/m ²	γ	$\dot{q}_w^\downarrow = \dot{q}_{cond} + \dot{q}_{rad}$ kW/m ²	γ
T1	AISI 316L	169	$1.051 \cdot 10^{-2}$	199	$4.149 \cdot 10^{-2}$
T2	MTA C/SiC	203	$8.431 \cdot 10^{-3}$	206	$8.797 \cdot 10^{-3}$

7. Concluding remarks and perspectives

A methodology to rebuild the thermal steady-state of the sample probe subjected to the plasma flow has been proposed and applied to relevant test cases on metallic and ceramic specimens. A finite element thermal model for the test probe was developed, highlighting the importance of carefully accounting for temperature dependent thermal properties and contact resistance effects. The VKI Plasmatron experimental set-up was improved, introducing a geometrical calibration procedure applied to IR thermography to extract quantitative temperature data over non-planar test objects. The proposed analysis is based on:

- an auxiliary experiment to extract the heat flux profile shape over the probe surface;
- the actual material test, with suitable measurements necessary to feed the IHTP;
- the solution of the IHTP by means of recursive least square approach, minimizing the difference between computed and measured temperatures.

Results showed close agreement with the IR temperature measurements in absolute value; thermocouple data, instead, had to be normalized to a reference value, due to a systematic bias with respect to the radiometric temperature measurements. In particular, for the highly catalytic stainless steel specimen, the thermal interaction revealed significant, corresponding in average to almost 30% of the total heat rate released from the gas to the surface. However, radial increase in the heat flux leads to a lower conduction around the stagnation region, where only $\sim 18\%$ was estimated. On the other hand, the low-catalytic ceramic specimen was affected by negligible heat exchange with the probe body ($\sim 8\%$ in average and only $\sim 1.5\%$ at stagnation point). As a practical application of the study, the additional information provided by thermal analysis was applied to the determination of the material catalytic coefficient. Considerable difference was noticed for the metallic specimen when conduction inside the material sample was accounted for.

The parameters which seem to influence the most heat conduction in the sample are the catalytic transition between the sample and the probe cover, along with the thermal conductivity of the sample material. In particular, the diffusive heat flux to the surface can undergo a significant variation, leading to a large temperature difference between the two probe components. This, along with the larger conductivity of the metallic specimen, leads to significant heat loss on the side for the stainless steel sample. On the other hand, the lower catalytic coefficient and thermal conductivity of the carbon ceramic material make heat conduction negligible.

The suggested methodology is suitable for a broad range of applications, as far as the thermal steady-state is reached. However, extension to the transient thermal phase could be problematic, since time resolved heat fluxes are more difficult to estimate. Moreover, one main assumption underlying the thermal analysis is that the heat flux profile shape over the probe surface is dependent on two parameters only. Numerical simulations of the flow field, for instance, could provide a closer insight in the actual transition of the diffusive and convective heat fluxes when adjacent materials show different catalytic properties. The problem of the systematic bias between thermocouple and radiometric measurements should be addressed in a dedicated study, to accurately quantify and correct the measurement errors. In conclusion, a sensitivity analysis to the model input parameters should be performed, showing the effect of the measurement uncertainties in the estimation of the thermal interaction and highlighting the most relevant quantities to consolidate the model.

8. Acknowledgments

The research of A. Fagnani is supported by a fellowship awarded by the Research Foundation Flanders (FWO #1SB3219N). Pascal Collin is acknowledged for his valuable help as Plasmatron operator.

References

- [1] F. Avallone, C. S. Greco, F. F. J. Schrijer, and G. Cardone. A low computational-cost inverse heat transfer technique for convective heat transfer measurements in hypersonic flows. *Experiments in Fluids*, 56:56–86, 2015.
- [2] M. Balat-Pichelin and P. Omary. Study of the atmospheric entry of metallic space debris - oxidation and emissivity evaluation to contribute to "design for demise". In *Proceedings of the 8th European Symposium on Aerothermodynamics for Space Vehicles*, 2015.
- [3] N. P. Bansal and J. Lamon. *Ceramic matrix composites materials, modeling and technology*. Wiley, 2015.

- [4] P. Barbante and O. Chazot. Flight extrapolation of plasma wind tunnel stagnation region flowfield. *Journal of Thermophysics and Heat Transfer*, 20(3):493–499, 2006.
- [5] P. F. Barbante. *Accurate and Efficient Modelling of High Temperature Nonequilibrium Air Flows*. PhD thesis, von Karman Institute for fluid dynamics, Université Libre de Bruxelles, 2001.
- [6] P. F. Barbante, G. Degrez, and G. S. R. Sarma. Computation of nonequilibrium high temperature axisymmetric boundary-layer flows. *Journal of Thermophysics and Heat Transfer*, 16(4):490–497, 2002.
- [7] L. Barka, M. Balat-Pichelin, J. L. Sans, J. Annaloro, and P. Omaly. Influence of oxidation and emissivity for metallic alloys space debris during their atmospheric entry. In *In Proc. 7th European Conference on Space Debris, Darmstadt, Germany*, 2017.
- [8] J-Y. Bouguet. Camera calibration toolbox for matlab. Available at: <http://www.vision.caltech.edu/bouguetj>. Accessed on 2019-05.
- [9] G. Cardone. IR heat transfer measurements in hypersonic plasma flows. *QIRT journal*, 4(2):233–251, 2007.
- [10] G. Cardone, A. Ianiro, G. dello Ionio, and A. Passaro. Temperature maps measurements on 3D surfaces with infrared thermography. *Experiments in Fluids*, 52:375–385, 2012.
- [11] S. Caristia, F. De Filippis, A. Del Vecchio, and E. Graps. SCIROCCO PWT Facility for High Temperature Materials Assembly Testing. In *12th AIAA International Spaces Planes and Hypersonic Systems and Technologies*, Bremen, Germany, 2003. AIAA.
- [12] G. M. Carlomagno and G. Cardone. Infrared thermography for convective heat transfer measurements. *Experiments in Fluids*, 49:1187–1218, 2010.
- [13] G. M. Carlomagno, L. de Luca, G. Cardone, and T. Astarita. Heat flux sensors for infrared thermography in convective heat transfer. *Sensors*, 14:21065–21116, 2014.
- [14] O. Chazot, R. Régnier, and M. A. Garcia. Simulation methodology in plasmatron facility and hypersonic wind tunnels. *12th International Conference on Methods of Aerophysical Research*, pages 87–92, 2004.
- [15] M. J. Colaco, H. R. B. Orlando, and G. S. Dulikravich. Inverse and optimization problems in heat transfer. *Journal of the Brazilian Society of Mechanical Science & Engineering*, 28(1):1–24, 2006.
- [16] A. Fagnani. Plasma testing methodology for demise phenomena analysis. Master’s thesis, VKI PR 2018-05, 2018.
- [17] J. A. Fay and F. R. Riddell. Theory of stagnation point heat transfer in dissociated air. *Journal of Aeronautical Science*, 25(2):73–85, 1958.
- [18] R. Goulard. On catalytic recombination rates in hypersonic stagnation heat transfer. *Jet Propulsion*, 28(11):737–745, 1958.
- [19] C. K. Gupta. *Materials in Nuclear Energy Applications, Volume II*. CRC Press, 2018.
- [20] F. Hecht. New development in freefem++. *Journal of Numerical Mathematics*, 20(3-4):251–265, 2012.
- [21] J. Heikkilä. Geometric camera calibration using circular control points. *IEEE Transactions on Pattern Analysis and Machine Intelligence*, 22(10):1066–1077, 2000.
- [22] B. Helber. *Material Response Characterization of Low Density Ablators in Atmospheric Entry Plasmas*. PhD thesis, von Karman Institute for Fluid Dynamics & Vrije Universiteit Brussel, 2016.
- [23] T. W. Kerlin and M. Johnson. *Practical thermocouple thermometry, 2nd edition*. International Society of Automation, 2012.
- [24] P. G. Klemens and G. Neuer. *Numerical Data and Functional Relationships in Science and Technology, Vol. 15, subvolume C, Thermal Conductivity of Pure Metals and Alloys*. Springer Verlag, Berlin, 1991.
- [25] A. F. Kolesnikov. Condition of Simulation of Stagnation Point from High Enthalpy Flow. *Fluid Dynamics*, 28(1):131–137, 1993.

PROBE-MATERIAL THERMAL INTERACTION IN PLASMA WIND TUNNEL TESTS

- [26] R. W. Lewis, K. Morgan, H. R. Thomas, and K. N. Seetharamu. *The Finite Element Method in Heat Transfer Analysis*. John Wiley & Sons, 1996.
- [27] J. IV Lienhard and J. V Lienhard. *A heat transfer textbook, 4th edition*. MIT press, 2017.
- [28] Thierry Magin. *A Model for Inductively Coupled Plasma Wind Tunnels*. PhD thesis, von Karman Institute for FLuid Dynamics & Université Libre de Bruxelles, 2004.
- [29] J. T. Nakos. Uncertainty analysis of thermocouple measurements used in normal and abnormal thermal environment experiments at Sandia's radiant heat facility and Lurance Canyon Burn site. Technical report, Sandia National Laboratories report SAND2004-1023, 2004.
- [30] M. N. Ozisik and H. R. B. Orlande. *Inverse heat transfer: fundamentals and applications*. CRC Press, Boca Raton, 2000.
- [31] F. Panerai. *Aerothermochemistry Characterization of Thermal Protection Systems*. PhD thesis, von Karman Institute for Fluid Dynamics & Università degli Studi di Perugia, 2012.
- [32] D. Vanden Abeele and G. Degrez. Efficient computational model for inductive plasma flows. *AIAA Journal*, 38(2):234–242, 2000.
- [33] M. Vollmer and K.-P. Mollmann. *Infrared Thermal Imaging*. Wiley, 2010.
- [34] P. M. B. Waswa, M. Elliot, and J. A. Hoffman. Spacecraft design-for-demise implementation strategy & decision-making methodology for low earth orbit missions. *Advances in Space Research*, 51:1627–1637, 2013.
- [35] Prévereaud Y., J. L. Vérand, M. Balat-Pichelin, and J.-M. Moschetta. Numerical and experimental study of the thermal degradation process during the atmospheric re-entry of a TiAl6V4 tank. *Acta Astronautica*, 122:258–286, 2016.